Chapter 10: Modeling of Stiffness, Strength, and Structure–Property Relationship in Crosslinked Silica Aerogel

Samit Roy and Awlad Hossain

Department of Aerospace Engineering and Mechanics, The University of Alabama, Tuscaloosa, AL 35487, USA

10.1 Introduction

Mechanically stable forms of lightweight materials with porosities up to 98% were first introduced in the form of silica aerogels in the 1930s. Recently, interest in aerogels and other lightweight materials in engineering applications have increased tremendously. Native silica aerogels are chemically inert, low-density, nanostructured porous materials with poor mechanical properties. They are the product of the sol–gel process whose final step involves extracting the pore-filled solvent with liquid carbon dioxide through supercritical drying. Practical applications of native aerogels are somewhat limited as they are brittle and hygroscopic, absorbing moisture from the environment which eventually leads to aerogel collapse due to capillary forces in the pores. Nevertheless, it has been recently discovered that crosslinking the nanoparticle building blocks of silica aerogels with polymeric tethers increases both modulus and strength significantly [4]. Along these lines, a novel, multifunctional, crosslinked silica aerogel, to be

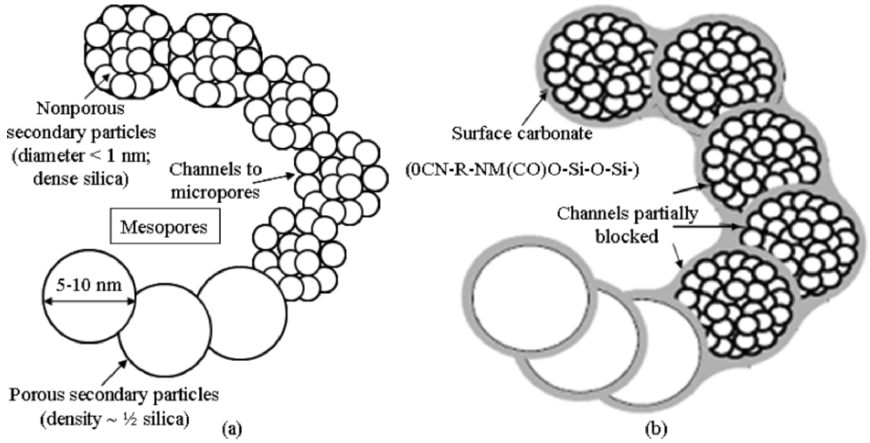

Fig. 10.1. (**a**) Silica aerogel structure before crosslinking and (**b**) x-aerogel structure after crosslinking [6]

referred to as *x-aerogel*, is derived by coating and encapsulating the skeletal framework of amine-modified silica aerogels with polyurea as depicted in Fig. 10.1.

Aerogels are reported to be one of the best thermal insulators. When sandwiched between two glass layers, aerogels reduce heat loss coefficient by more than a factor of 10, while preserving the capability of moderately high light transmission [5]. Aerogels are being considered for different aerospace applications, such as a thermal protection system (TPS), catalyst support, or as hosts for a variety of functional materials for chemical, optical, and electronic devices.

Cylindrical samples of x-aerogel manufactured in the author's laboratory are shown in Fig. 10.2. It was observed from the mechanical characterization tests that x-aerogel has very good compressive, tensile, and shear properties, in addition to its low thermal conductivity [4, 6, 8]. Recently, manufacturing of a lightweight cryogenic propellant tank with low thermal conductivity has been proposed using novel x-aerogel material. While the use of composite sandwich panels for cryotanks is not novel, it is feasible that the delamination of facesheet from the core due to cryo-pumping, analogous to the failure that occurred in the X-33 prototype, could perhaps be prevented through the use of x-aerogel core instead of a standard honeycomb core.

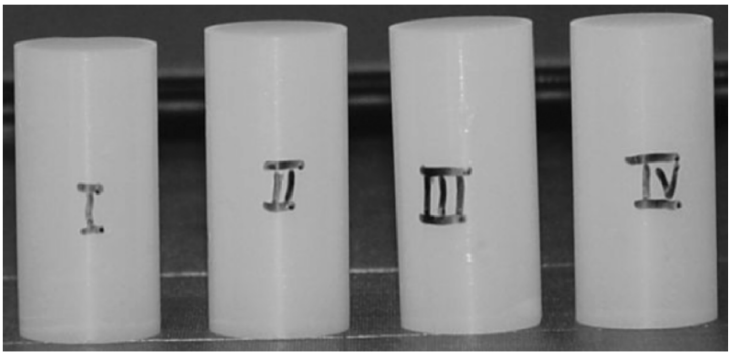

Fig. 10.2. Cylindrical samples of x-aerogel

It is envisioned that aerogel material can be used as the central core bonded between two facesheets of a sandwich plate. As aerogels are highly porous, facesheets will be necessary to make the sandwich composite panels impermeable for storing cryogenic fuels. Facesheets can be made of carbon fiber-reinforced polymer (CFRP) having high tensile load-bearing capability. Schematics of a typical sandwich plate with a standard honeycomb core and an x-aerogel core at the center are shown in Fig. 10.3. As another example of a practical application of x-aerogel, a conceptual design of a prototype cryogenic propellant tank using x-aerogel material is shown in Fig. 10.4.

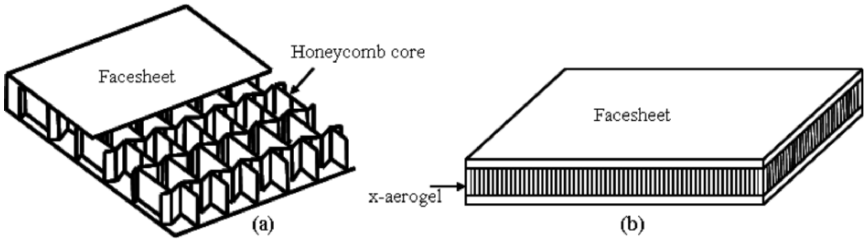

Fig. 10.3. (**a**) Traditional sandwich panel with honeycomb core and (**b**) novel sandwich panel with x-aerogel as central core material

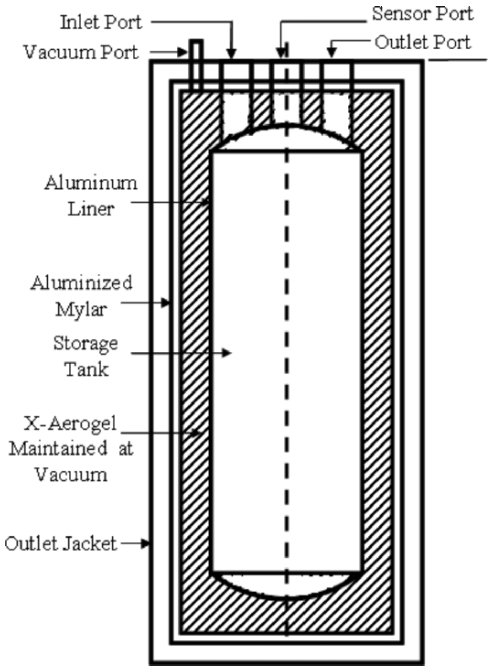

Fig. 10.4. Prototype cryotank design concept with x-aerogel material

10.2 Nanostructural Features of Silica Aerogel

Aerogel is a class of monolithic material that possesses porous structure. Scanning electron microscopy (SEM) [1] and transmission electron microscopy (TEM) [9] are widely used to produce direct images of mesoporous structures. For the crosslinked silica aerogel, SEM imaging was conducted for different loading stages, as shown in Fig. 10.5. In this figure, the clusters of secondary nanoparticles are clearly visible along with the mesopores.

The mechanical, thermal, electrical, and optical properties exhibited by x-aerogels are related to their mesoporous cluster assemblies, as depicted earlier in Fig. 10.1. The sol–gel manufacturing process can control the geometry, porosity, and physical properties of mesoporous silica aerogels by manipulating its chemistry and processing parameters. The stiffness and strength of x-aerogels strongly depend on their microstructural features, such as particle connectivity. However, there is no experimental technique currently available to measure this connectivity directly. As an alternative metric, the self-similar characteristics of aerogel structures can be investigated by evaluating their fractal dimension from geometric correlations.

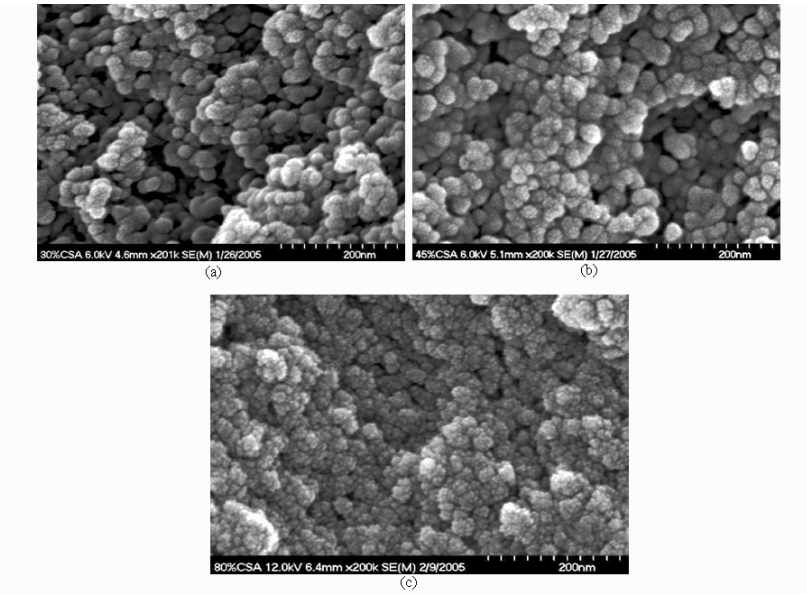

Fig. 10.5. SEM images of crosslinked silica aerogels. The clusters of secondary nanoparticles (*round particles*) and the mesopores (*dark spots*) are clearly visible: (**a**) 30% strain – no appreciable change in mesoporous structure, (**b**) 45% strain – gradual decrease in the mesoporosity, few dark spots, and (**c**) 77% strain – appreciable loss of porosity, particles are squeezed closer to one another

The shape of clusters or cluster configuration, the existence of voids of all sizes, and the gradual loss of connectivity among mesoporous particles suggest that a fractal dimension can be attributed to the x-aerogel structures as a useful descriptive parameter [5]. The fractal dimension of a mesoporous structure can be determined from its particle orientation within a sphere of a given radius or from the slope of a radial distribution function. It was reported in the literature [5] that not only the mass of aerogel but also other properties, such as vibrational dynamics, scale according to aerogel's fractal dimension. In general, due to its inherent porosity, the aerogel morphology represents a fractal dimension of less than 3; and its fractal dimension decreases with decreasing cluster densities, as presented later in this chapter.

In this study, a three-dimensional distinct element analysis (DEA) simulation was performed to determine the structure–property relationship of nanostructured x-aerogel material. The model attempted to incorporate microscale effects – such as particle bond stiffness, bond strength, particle frictional coefficient, initial cluster porosity (or density), and density of

secondary silica particles – into a macroscale structure–property relationship for the prediction of Young's modulus and strength. In addition, numerical analyses were carried out to determine the fractal dimension of the aerogel structure while varying its initial cluster porosity or density. Modeling methodology will provide insights for both stiffening and strengthening mechanisms and how these mechanisms can be optimized with minimum weight penalty. Therefore, it is envisioned that numerical modeling will greatly reduce the number of "trial-and-error" experiments necessary to further enhance the properties of this novel material.

10.3 Particle Mechanics for Numerical Modeling of Aerogels

Various researchers have developed different cluster aggregation algorithms for simulating structural characterizations of mesoporous materials. Diffusion-limited cluster aggregation (DLCA) and reaction-limited cluster aggregation (RLCA) algorithms are some examples [7]. A DLCA technique was first developed by a research group at Harvard University to interpret scattering experiments and subsequently used for understanding different phenomenon related to porous media, such as gelation, fractal studies, and scattering spectroscopy. The DLCA algorithm proceeds with random filling of a three-dimensional cubic volume with nonintersecting spheres. The diameters of these spheres are chosen from a Gaussian distribution function. These spheres are then set to diffuse inside the cubic boundary. When in motion, a particle is tested against overlapping with neighboring particles. If an overlap is detected, then that particle is merged to neighboring particles to form a new cluster. The diffusive motion is completed once all the particles have merged to form a single cluster. The process of aggregation is depicted schematically in Fig. 10.6. A cluster of three particles is moved and tested for an overlap with neighboring particle as shown in Fig. 10.6a. Once an overlap is detected, this cluster is aligned to the neighboring particle as shown in Fig. 10.6b. Then, this cluster and particle are merged to form another cluster of four particles as shown in Fig. 10.6c. This process continues until all particles have merged to form a final single cluster. After the network connectivity has been determined among the particles using DLCA, this information is transferred to the DEA software. Finally, the DEA can be used to determine the structure–property relationship through numerical simulation.

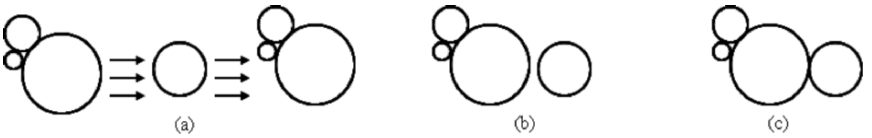

Fig. 10.6. Aggregation process for particles in DLCA

A particle flow code in three dimensions (PFC^{3D}) [3] simulates mechanical behavior of mesoporous structures when a bonded assembly of spherical particles is available from DLCA, as described earlier. PFC^{3D} is classified as a discrete or distinct element analysis code as it allows finite displacements and rotations of discrete bodies and recognizes new contacts automatically. PFC models are categorized as direct damage-type numerical models in which deformation is not a function of prescribed relationships between stress and strain but of changing microstructure. The numerical model is composed of distinct particles that displace independently from one another and interact only at contacts. Newton's laws of motion provide the fundamental relations between particle motion and forces. The complex nature of mesoporous structures can be modeled by bonding particles together at their contact points and allowing the bond breakage for excessive loading to exceed the bond strength. The PFC^{3D} conducts a particle flow model with the following assumptions:

1. The particles are treated as rigid bodies and are spherical in shape. The deformation of a packed-particle assembly results primarily from the sliding and rotation of rigid particles and not from the individual particle deformation.
2. Particles are in contact with each other. Contacts among the particles occur over a vanishingly small area, i.e., at a point, where bonds can exist.
3. Behavior at contacts uses a soft-contact approach wherein the particles are allowed to overlap one another at contact points.
4. The magnitude of the overlap is related with contact force via the force–displacement law, and all overlaps are small enough compared to particle sizes.

In addition to spherical particles (referred to as "balls"), the PFC^{3D} includes "walls" to apply velocity boundary conditions for compaction and confinement of particle assemblies. The balls and walls interact with one another via forces that arise at contacts. The equations of motion are satisfied

for each ball; however, they are not satisfied for each wall, i.e., forces acting on a wall do not influence its motion. Instead, its motion is specified by the user and remains constant regardless of the contact forces acting upon it.

The calculation cycle in PFC^{3D} is a time-stepping algorithm that requires repeated applications of the laws of motion to each particle, a force–displacement law to each contact, and an updating of wall positions. Contact among particles forms and breaks automatically during the course of a simulation. The calculation cycle is shown in Fig. 10.7. At the start of each time step, a set of contacts is updated from known particle and wall positions. The force–displacement law is then applied to each contact to update contact forces. Next, the law of motion is applied to each particle to update its velocity and position. The constitutive behavior used in PFC^{3D} is mainly represented by contact models which, in essence, describe physical behavior at each contact by stiffness, slips, and bonding models.

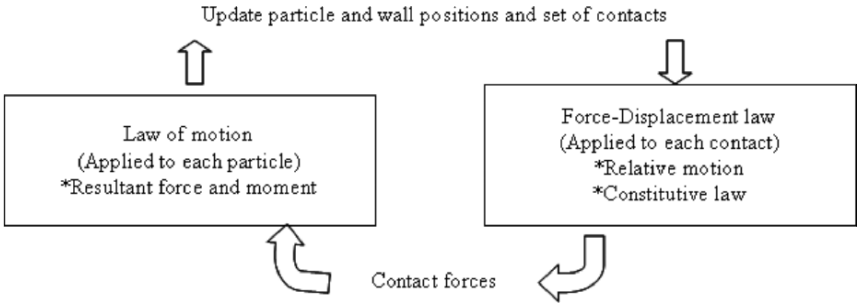

Fig. 10.7. Calculation cycle used in PFC^{3D} [3]

The contact stiffness relates contact forces and relative displacements in normal and shear directions. The normal stiffness is a secant stiffness since it relates total normal force to total normal displacement. The shear stiffness represents a tangent stiffness as it relates the shear force and displacement in incremental form. The normal and shear stiffness are expressed in (10.1) and (10.2), respectively

$$P_{\mathrm{n}} = k_{\mathrm{n}} v_{\mathrm{n}}, \tag{10.1}$$

$$\Delta P_{\mathrm{s}} = k_{\mathrm{s}} \Delta v_{\mathrm{s}}. \tag{10.2}$$

Here, P, k, and v indicate force, stiffness, and particle velocity, respectively. Subscripts n and s represent normal and shear components, respectively.

If the contact normal stiffness is altered during the course of simulation, there will be an immediate effect upon the entire assembly. Whereas, if the shear stiffness is altered, it will only affect the new increment of shear force. Two stiffness models, linear and Hertz–Mindlin, are available in PFC^{3D} for representing linear and nonlinear relations between force and displacement, respectively. The slip model in PFC^{3D} allows two entities in contact to slide relative to one another. A separation occurs if they are not bonded and a tensile force develops between them. The slip condition exists when the shear component of force reaches its maximum limit.

PFC^{3D} allows particles to be bonded together at contacts and supports two types of bonding models: a contact-bond model and a parallel-bond model. Both bonds can be envisioned as a kind of glue joining two particles. The contact-bond glue is of a vanishingly small radius that acts only at the contact point, while the parallel-bond glue is of a finite radius that acts over a circular cross-section lying between the particles. The contact bond can only transmit a force, while the parallel bond can transmit both a force and a moment. Both types of bonds may be active at the same time; however, the presence of a contact bond inactivates the slip model. The bonding logic is illustrated in Fig. 10.8.

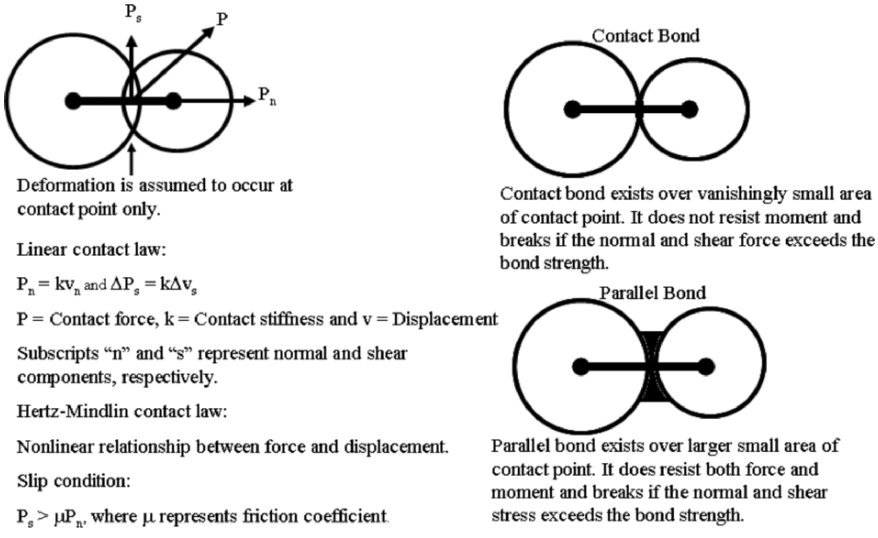

Fig. 10.8. Contact and parallel bonding logics used in PFC^{3D} [3]

Properties related to particles and their corresponding contacts are required to perform a simulation in PFC^{3D}. The response of a mesoporous material is mainly affected by particle size and packing arrangement. Therefore, the model parameters cannot be related directly to a set of relevant material properties. The relation between PFC model parameters and commonly measured material properties is only known a priori for certain simple packing arrangements. In case of arbitrary packing or particle assemblage, the relation is found by means of a calibration process where repeated simulations are required to mimic the true material responses. The user needs to specify parameters related with particle contact stiffness, particle friction coefficients, bond strengths, and others to simulate a corresponding set of macroresponses, such as elastic constants and peak strength envelope, etc. To get a rough estimate of particle contact stiffness and bond strength, PFC^{3D} provides the following two equations

$$E = \frac{k_{\mathrm{n}}}{4R}, \tag{10.3}$$

$$\sigma_{\mathrm{t}} = \frac{s_{\mathrm{n}}}{4R^2}, \tag{10.4}$$

where E is the Young's modulus of the particle assembly as obtained from laboratory tests, k_{n} is the normal contact stiffness of the particles, R is the particle radius, σ_{t} is the measured tensile strength of the particle assembly, and s_{n} is the normal bond strength in particle contacts. The shear components of stiffness and bond strength k_{s} and s_{s} are taken to be some fraction or equal to their respective normal components. These two relations are derived for a cubic array of particles, which may not be a correct representation of the actual particle arrangement in laboratory samples. Nevertheless, these equations provide useful information that could be used to obtain first estimates of the micromechanical parameters. A flowchart is provided in Fig. 10.9 to help the reader better understand the simulation process.

10.4 Materials Characterization of X-Aerogel Through Compression Experiments

Compression experiments were performed to obtain material responses of x-aerogel specimens, which were subsequently used to verify the numerical results obtained from PFC^{3D}. During the experiments, aerogel samples were

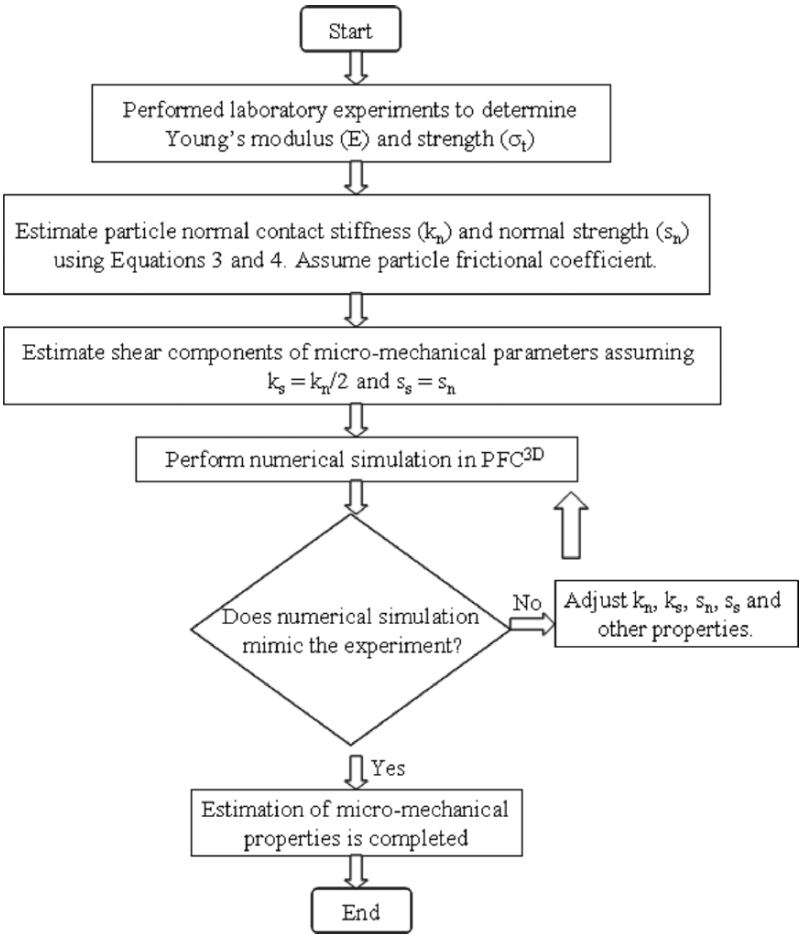

Fig. 10.9. Flowchart of the simulation process in PFC^{3D}

prepared following the procedures described in [8]. Compression experiments were conducted under different temperature conditions to study their corresponding effects on the measured properties. Cylindrical specimens consistent with ASTM D695-02a standard were used in an MTS machine equipped with a 55,000 lb load cell. Five replicate samples were tested. A typical experimental setup is shown in Fig. 10.10. Separate sets of samples were loaded at strain rates of 0.0035, 0.035, and 0.35 s^{-1} to investigate strain rate effects in x-aerogel.

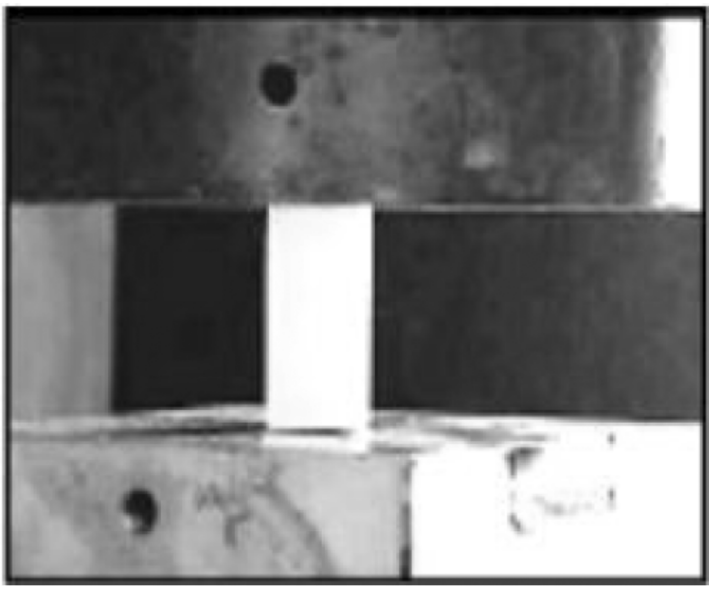

Fig. 10.10. Uniaxial compression testing of crosslinked silica aerogel

Figure 10.11 represents the average stress–strain response for crosslinked silica aerogel specimens under compressive loading at room temperature at a strain rate of 0.0035 s^{-1}. Data for compressive yield strength, compressive stress at ultimate failure, and Young's modulus for individual sample calculated at room temperature, as well as the average values with their standard deviations, are summarized in Table 10.1. The ultimate compressive strength with other properties of native (uncrosslinked) silica aerogel is given in Table 10.2 for comparison.

During the compression test, crosslinked aerogels were found to behave as linearly elastic under small strains (<4%) and then exhibited yield (until ~40% compressive strain), followed by densification and inelastic hardening. Aerogel samples ultimately failed at approximately 77% compressive strain, yielding an ultimate compressive strength of 186 ± 22 MPa. The average yield stress defined at the beginning of densification was 4.26 ± 0.25 MPa and occurred at approximately 4% strain.

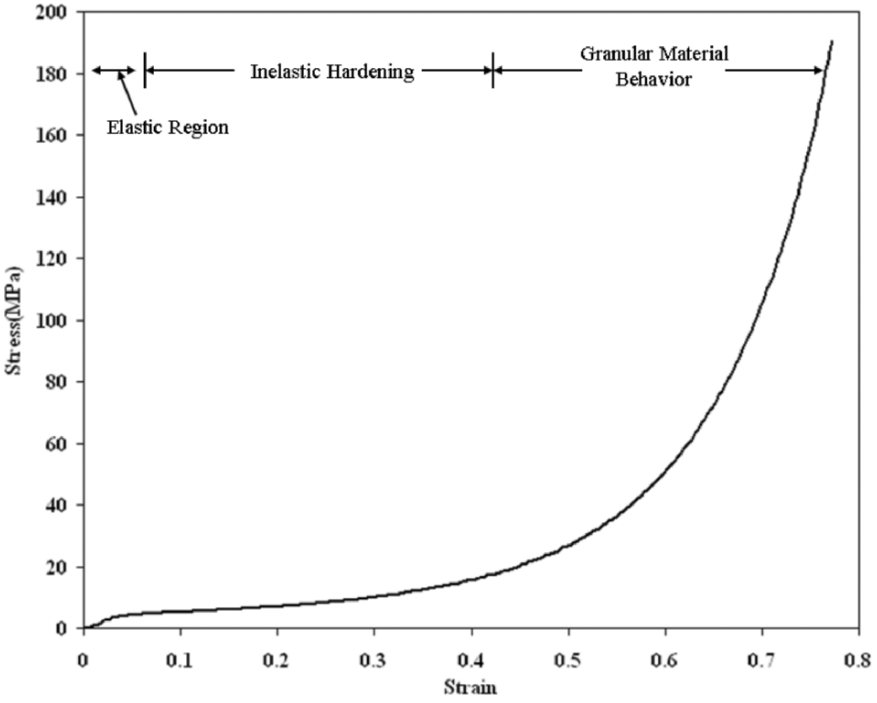

Fig. 10.11. Stress–strain curve in uniaxial compression on crosslinked silica aerogel

Table 10.1. Summary of compressive strength data of isocyanate crosslinked silica aerogels at a strain rate of 0.0035 s^{-1}

Sample number	Density (g cc^{-1})	Compressive yield strength (MPa)	Compressive strength (MPa)	Failure strain (%)	Young's modulus (MPa)
1	0.48	4.19	190.33	77.22	122.85
2	0.47	4.25	222.08	77.04	119.58
3	0.48	3.88	168.55	77.20	126.27
4	0.48	4.47	173.72	76.10	135.27
5	0.48	4.50	173.20	78.35	138.94
Average	0.478 ± 0.004	4.26 ± 0.25	186 ± 22	77.2 ± 0.8	129 ± 8

Table 10.2. Summary of compressive strength data of native silica aerogels at a strain rate of 0.0035 s^{-1}

Sample number	Density (g cc^{-1})	Ultimate compressive strength (MPa)	Failure strain (%)	Young's modulus (MPa)
1	0.18	4.0	5.31	96.7
2	0.20	4.1	6.00	86.9
Average	0.19 ± 0.01	4.1 ± 0.07	5.66 ± 0.49	92 ± 7

Table 10.3 compares the absolute and specific compressive strengths of crosslinked aerogel with other materials. The specific compressive strength of crosslinked aerogel is higher than that of steel, aluminum, and fiber-glass, and is comparable to that of aerospace grade graphite composite. The relatively high specific compressive strength at ultimate failure combined with low thermal conductivity would render crosslinked silica aerogel attractive as multifunctional material for various space applications, such as cryogenic fuel tanks.

Table 10.3. Comparison of compressive strength of crosslinked silica aerogel with other composite materials for engineering applications

Material	Density (g cc^{-1})	Compressive strength (MPa)	Specific compressive strength (N m kg^{-1})
E-glass epoxy[a]	1.94	550	283,000
Kevlar-49 epoxy[a]	1.30	280	215,000
T 300 epoxy[a]	1.47	830	564,000
VSB-32 epoxy[a]	1.63	690	423,000
GY-70 epoxy[a]	1.61	620	385,000
2024 T3 Al	2.87	345	120,000
7075T6	2.80	475	169,000
4130 steel	7.84	1,100	140,000
x-aerogel	0.48	186	389,000

[a]Fiber volume fraction, $V_f = 0.6$.

Young's modulus in compression was evaluated from the slope of initial linear portion (at <4% strain) of the stress vs. strain curve. The Young's modulus of the crosslinked aerogel was 129 ± 8 MPa compared to 92 ± 7 MPa of the native silica framework. The recovery (or spring back) behavior of crosslinked silica aerogels was characterized by conducting loading–unloading cycles along the stress vs. strain curve. A typical cylindrical sample was loaded and unloaded six times, first in the elastic region where deformation was completely recovered as shown in Fig. 10.12. Then it was unloaded and reloaded in the inelastic region where a hysteresis loop was always observed, presumably due to energy loss for bond breaking and slippage of polymer chains [2]. It was further noted that the percent strain recovery became progressively lower at higher strains, while in the inelastic hardened range (approximately 60% strain) there was virtually no strain recovery.

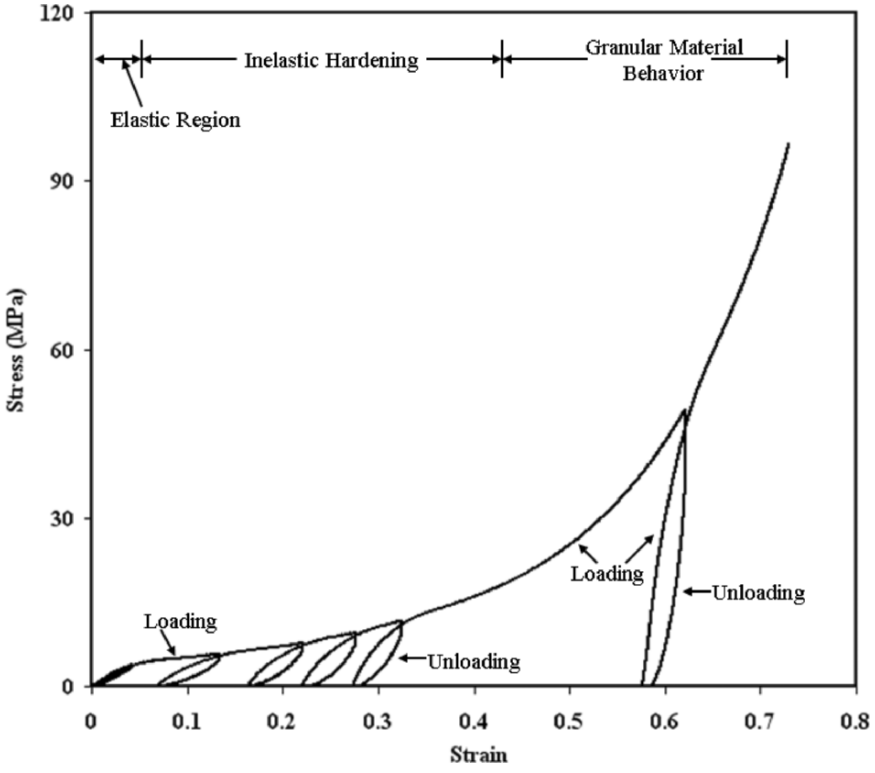

Fig. 10.12. Loading–unloading response of crosslinked silica aerogel

The changes in morphology of x-aerogel material under inelastic compression were evaluated by SEM, as shown earlier in Fig. 10.5. In this case, samples were loaded up to a predetermined strain. Then the load was removed and the samples were analyzed. Curiously, under SEM, the material did not show any noticeable difference in microstructure from its original state to 45% strain. Ultimately, SEM micrograph showed clear signs of collapse of the aerogel mesopores due to compaction, i.e., a nearly total loss of porosity, at failure (77% strain).

Finally, the effects of strain rate and temperature on ultimate compressive strength were evaluated. Figure 10.13 shows stress vs. strain curves at three different compressive strain rates of 0.0035, 0.035, and 0.35 s^{-1}. Although Young's modulus increased significantly with increasing strain rates (128, 160, and 205 MPa at strain rates of 0.0035, 0.035, and 0.35 s^{-1}, respectively), the shape of the overall stress vs. strain curves did not

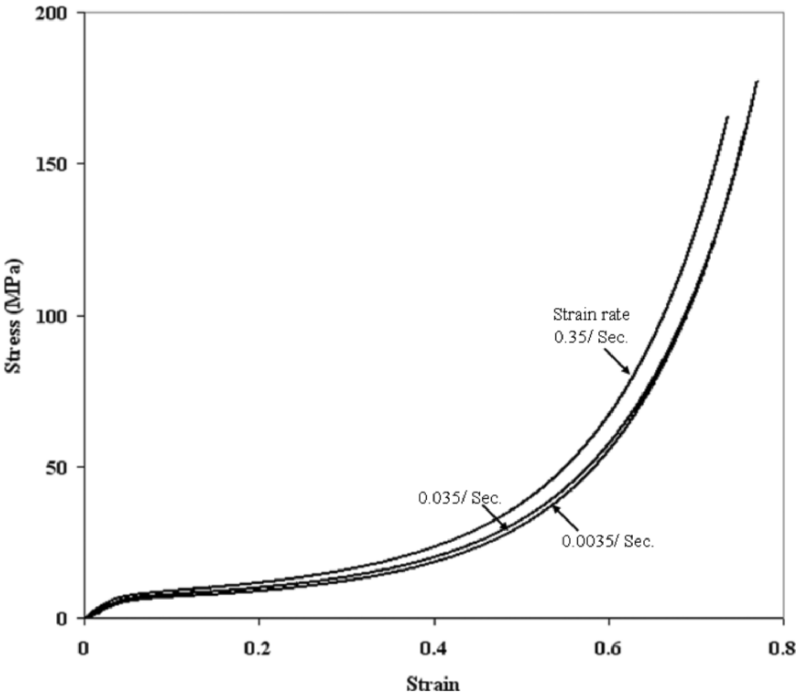

Fig. 10.13. Effect of strain rate on the behavior of crosslinked silica aerogel under uniaxial compression

change significantly. Therefore, within the strain rate range investigated, it can be stated that increasing strain rate does not have a deleterious effect on the energy-absorption behavior of crosslinked aerogels.

Figure 10.14 presents the compressive stress vs. strain curves for crosslinked aerogel samples that were tested at various temperatures. Mechanical response is essentially invariant of the temperature in the range between 21 and −55°C. However, the material stiffens significantly (the elastic modulus increases to ~450 MPa) and suffers premature compressive failure at cryogenic temperatures, e.g., −196°C. It should be noted that, due to a shortage of x-aerogel specimens, only one sample was available for this test. Additional cryogenic temperature tests are planned in the near future.

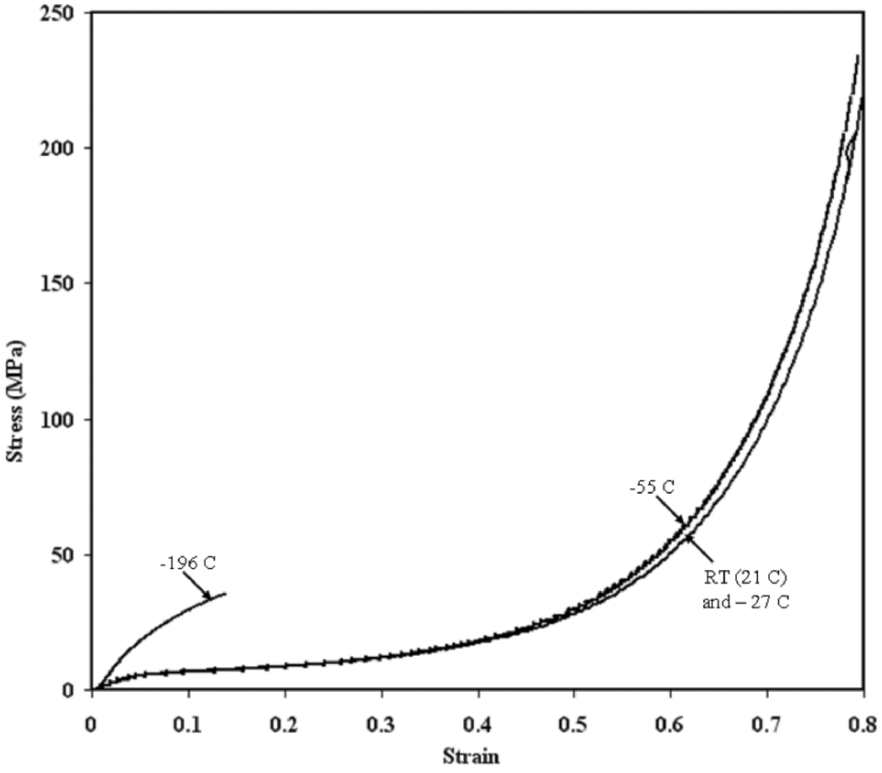

Fig. 10.14. Effect of temperature on the behavior of crosslinked silica aerogel under uniaxial compression

10.5 Numerical Simulation of Compression Experiment Using PFC^{3D}

Numerical simulation of compression experiment of crosslinked silica aerogel has been performed by using a PFC^{3D}, as described earlier. First, a cluster assemblage of spherical particles was generated, as shown in Fig. 10.15, using the DLCA algorithm. This algorithm randomly generates nonintersecting spherical particles according to a Gaussian distribution function. The DLCA provides the radius and location of each particle in a three-dimensional cubic space with a specified porosity. These values are then exported to PFC^{3D} (DEA code) as input data files.

The following section summarizes the necessary procedures or steps involved in a typical compression simulation using PFC^{3D}. Two separate data files can be used and executed in the command-driven mode during the simulation process. The first data file performs the following operations:

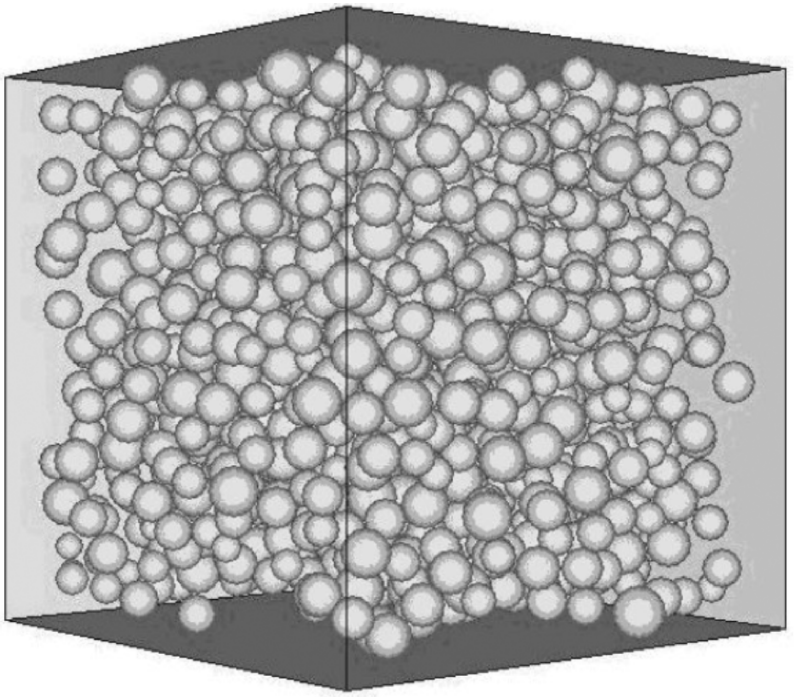

Fig. 10.15. Cluster assemblage of spherical particles generated by DLCA algorithm

- Define the boundary of the model, a three-dimensional cubic space, by defining the geometric locations of six walls or sides.
- Insert the cluster of nonintersecting spherical particles (balls) created by DLCA within the model boundary.
- Assign properties of spherical balls and boundary walls, which include ball density, friction coefficient, contact stiffness in normal and shear directions, contact-bond strength in normal and shear directions (in force unit), parallel-bond stiffness in normal and shear directions, parallel-bond strength in normal and shear directions, and wall stiffness in normal and shear directions.
- Apply gravitational force, if required.
- Assign the computational cycle number.
- Perform a number of calculation steps which monitor the ball movements and the change in unbalanced force as the assemblage is compacted. An equilibrium state has been reached when the unbalanced force converges to a value lower than the specified tolerance limit.
- Save the equilibrium state of assemblage that will be used by the second data file.

When the particle assemblage has reached an equilibrium state, the following operations are performed by the second data file:

- Restore the equilibrium state of particle assemblage confined by six fixed walls.
- Delete the fixed walls and define new top and bottom walls (moving) to compress the particle assemblage.
- Define the formulation for calculating average stress and strain based on force exerted on walls and wall movement, respectively.
- Assign wall properties, which include contact stiffness in normal and shear directions, friction coefficients, and wall velocities, to apply load in preferred direction.
- Save the history of average stress and strain. Plot the result and provide output file in desired format.

PFC^{3D} can be used in a fully predictive mode where enough data of high quality are available, or it can be used as a numerical laboratory to test design ideas in a data-limited system. Most of the aerogel modeling in this study is based on limited available data. In this study, various particle clusters were generated in DLCA varying aerogel initial cluster porosity from 70 to 80%. When the particle assemblage had been formed, it was compressed by two walls moving at opposite directions. All properties related with PFC^{3D} simulation are presented in Table 10.4 with their nominal values.

Table 10.4. Parameters used in PFC^{3D} simulation with nominal values

Properties	Description	Value
	Mass density	480 kg m^{-3}
	Contact stiffness in normal direction	150 N m^{-1}
	Contact stiffness in shear direction	150 N m^{-1}
	Radius multiplier for parallel bond	30×10^{-9}
	Parallel-bond normal stiffness per unit area	30×10^{15} N m^{-3}
Ball and bond	Parallel-bond shear stiffness per unit area	30×10^{15} N m^{-3}
	Parallel-bond normal strength	190×10^{6} Pa
	Parallel-bond shear strength	190×10^{6} Pa
	Contact-bond normal strength	3×10^{4} N
	Contact-bond shear strength	3×10^{4} N
	Friction coefficient	0.5
Fixed wall	Normal stiffness	1×10^{6} N m^{-1}
	Shear stiffness	1×10^{6} N m^{-1}
Moving wall	Normal stiffness	1×10^{15} N m^{-1}
	Shear stiffness	1×10^{15} N m^{-1}
	Friction coefficient	0.001
	Velocity in vertical (z) direction	0.1×10^{-10} m per step
Porosity	Initial cluster porosity	70–80%
Other Parameters	Number of particles (balls)	2,000–2,600
	Type of particles distribution	Gaussian
	Cell (3D box) size	$100 \times 100 \times 200$ nm

Snapshots of PFC^{3D} simulation at different compression stages are shown in Fig. 10.16. The bonds between particles break as the compressive load increases. Subsequently, secondary particles located at dead ends separate from the core assembly, as shown in Fig. 10.16. Numerical results for stress vs. strain were calculated and compared with experimental values. An excellent agreement was observed between the numerical and experimental results as shown in Fig. 10.17.

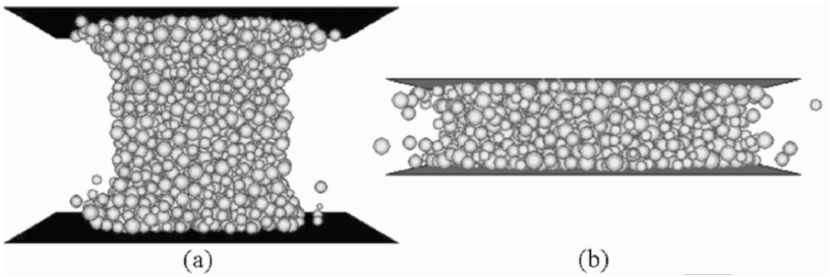

Fig. 10.16. Uniaxial compression simulation of aerogel (**a**) at 45% strain and (**b**) at 77% strain

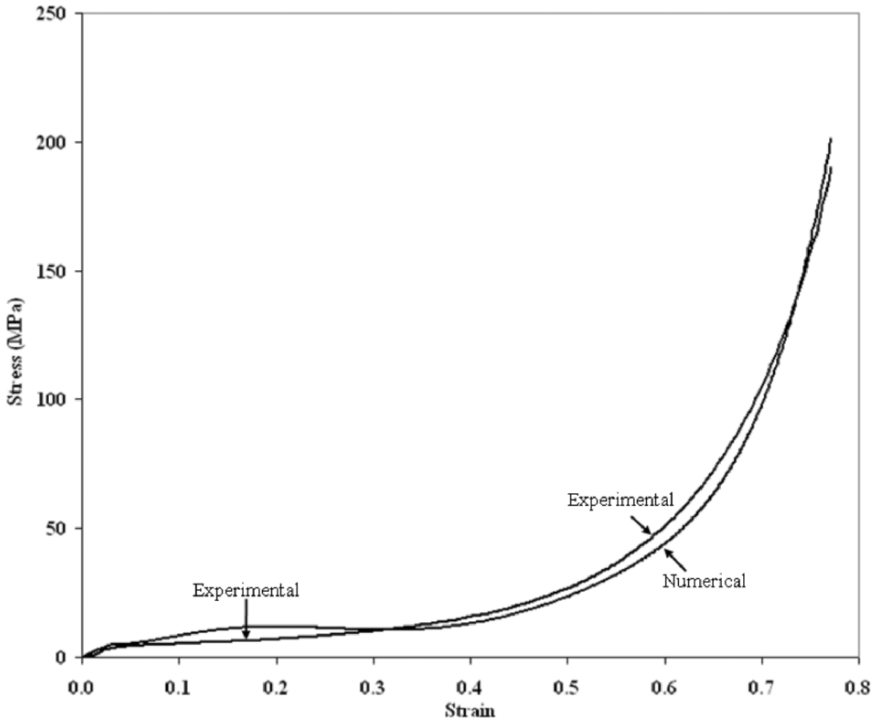

Fig. 10.17. Comparison between the experimental and numerical results

10.6 Parametric Sensitivity Analyses

Parametric sensitivity analyses were performed on the numerical model by varying one parameter at a time, while keeping the other parameters constant. The key parameters affecting the behavior of the numerical model

were identified by performing a few trial cases. The particle contact stiffness was found to be the most important parameter affecting the numerical results. Figure 10.18 shows the effect of increasing the contact stiffness, assuming both normal and shear stiffness are equal, on the stress vs. strain behavior. Not surprisingly, the modulus predicted by the numerical model was found to increase with increasing particle contact stiffness.

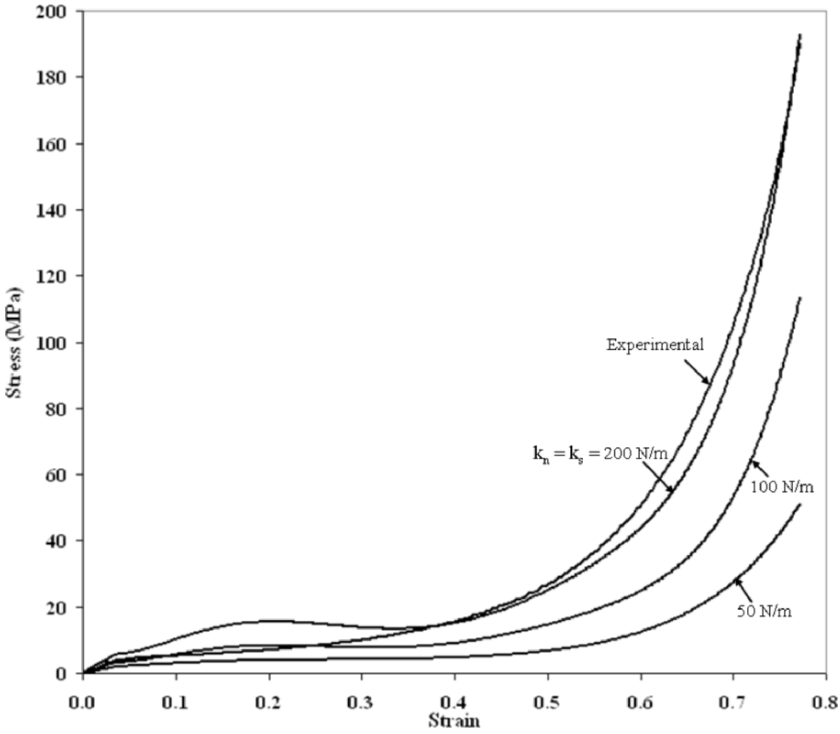

Fig. 10.18. Parametric sensitivity analyses with changing particle contact stiffness (N m^{-1}) equally in normal and shear directions

Parametric sensitivity analyses were then performed by changing the particle contact stiffness independently along the normal and shear directions. First, contact stiffness in the normal direction (k_n) was held constant at 150 N m^{-1} while the stiffness in shear direction (k_s) was varied. As shown in Fig. 10.19, numerical results did not change significantly with changes in the normal to shear stiffness ratio. However, a noticeable

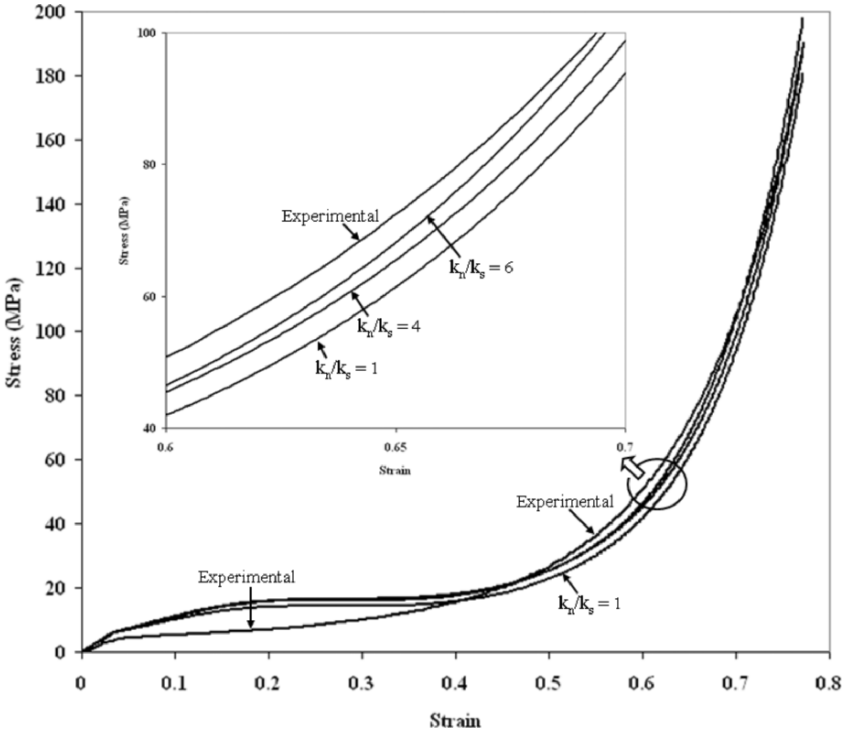

Fig. 10.19. Parametric sensitivity analyses with changing particle contact stiffness in shear direction while stiffness in normal direction was kept constant at 150 N m^{-1}

change was observed in stress vs. strain behavior when the particle contact stiffness in the shear direction (k_s) was held constant at 150 N m^{-1} and stiffness in the normal direction (k_n) was varied. As shear to normal stiffness ratio was increased, the numerical model was found to predict a significantly softer response, as shown in Fig. 10.20.

Particles used in PFC are not bonded among themselves by default. Particles in contact within a given range become bonded by assigning a bond strength. A bond breaks when force equals or exceeds the bond strength. In this parametric sensitivity study, the numerical simulation was repeated with varying bond strength. Bond breakage was found to be significantly reduced with increasing parallel-bond strength, as shown in Fig. 10.21, where each black patch represents a broken bond.

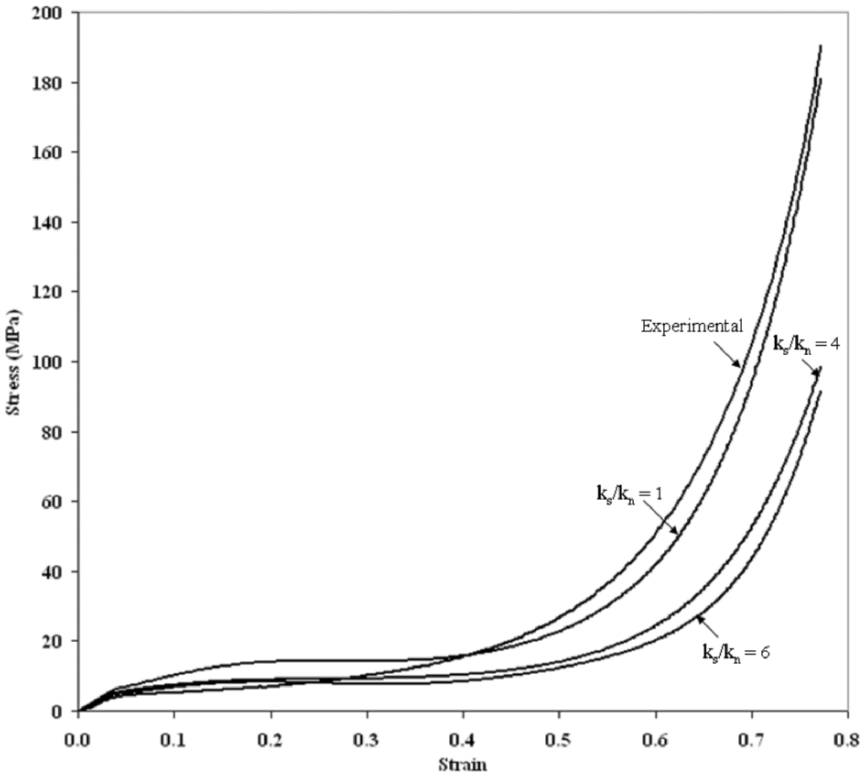

Fig. 10.20. Parametric sensitivity analyses with changing particle contact stiffness in normal direction while stiffness in shear direction was kept constant at 150 N m^{-1}

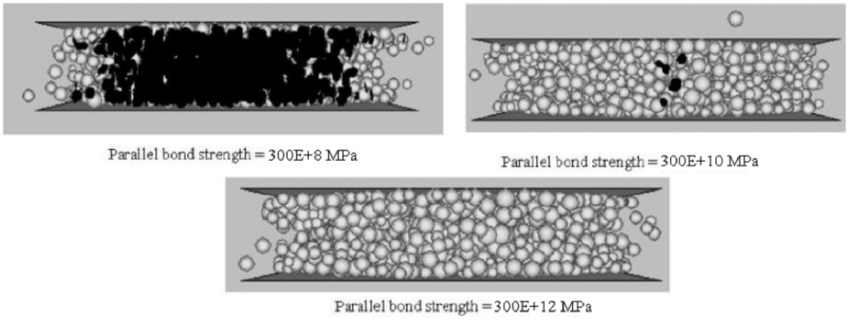

Fig. 10.21. Compressed particle clusters at 77% strain, where the *black spots* represent each bond breakage

Parametric sensitivity analyses were also performed to investigate the stress–strain response with changes in the particle frictional coefficient ranging from 0.01 to 1.0. The slope of the stress vs. strain curve in the granular region was found to increase as the frictional coefficient increased, as shown in Fig. 10.22. As the particle frictional coefficient increases, more force is required to compress the cluster, thereby stiffening the numerical model. Not surprisingly, there was very little effect of increasing particle mass density on the response of the stress vs. strain curve as shown in Fig. 10.23.

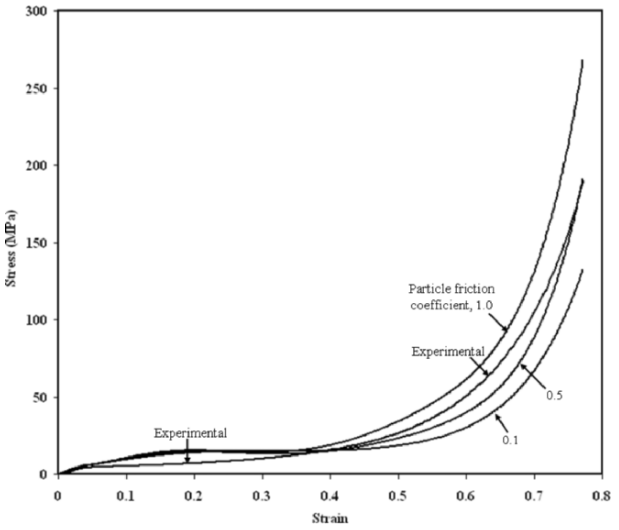

Fig. 10.22. Parametric sensitivity analyses with changing particle frictional coefficient

As mentioned earlier, the network connectivity of mesoporous aerogel structures consisting of nanosize particles can be investigated by evaluating their fractal dimension from initial cluster geometry. In this study, effort was directed to determining the fractal dimension of an aerogel structure by calculating the total number of particles within a specified spherical region [5], as expressed by (10.5) below:

$$d_{\mathrm{f}} = \frac{\mathrm{d}\ln N(r)}{\mathrm{d}\ln r}. \tag{10.5}$$

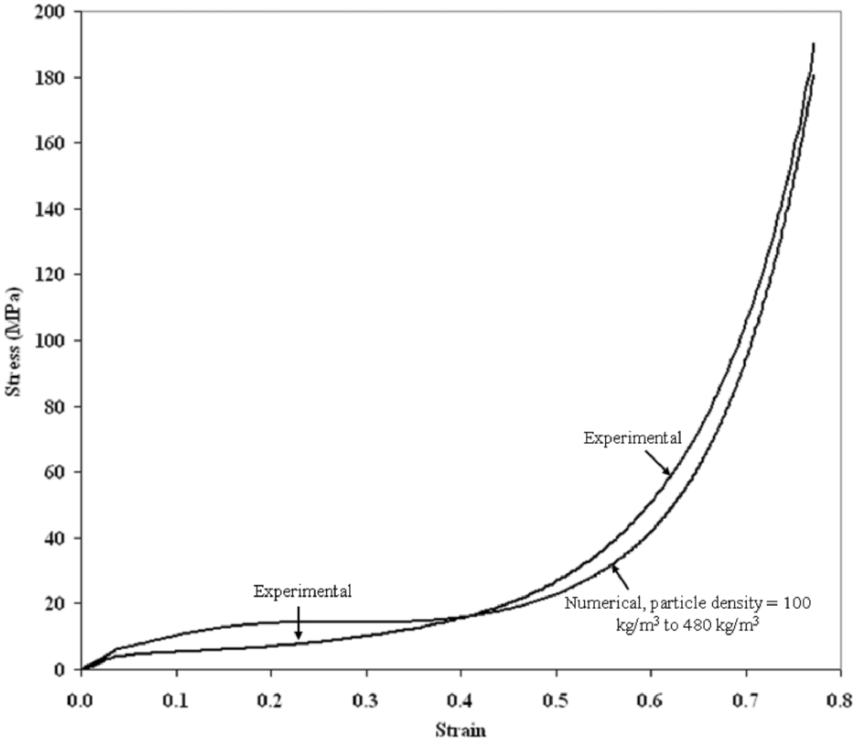

Fig. 10.23. Parametric sensitivity analyses with changing particle mass density (kg m^{-3})

Here, d_f represents the fractal dimension and $N(r)$ represents the total number of particles within a sphere of radius r, as shown in Fig. 10.24.

In Fig. 10.25, the total number of particles ($N(r)$) surrounding a reference point as a function of radial distance (r) in a double-logarithmic scale have been plotted. The different curves correspond to different initial cluster porosities, ranging from 70 to 80%, with clusters generated using DLCA. The fractal dimension (d_f) is evaluated as the slope of each line, as described in (10.5), and is indicated at the top of Fig. 10.25. This figure shows that aerogel structures with different initial cluster porosities have different fractal dimension. Therefore, each aerogel structure signifies a distinct network connectivity among the secondary nanoparticles.

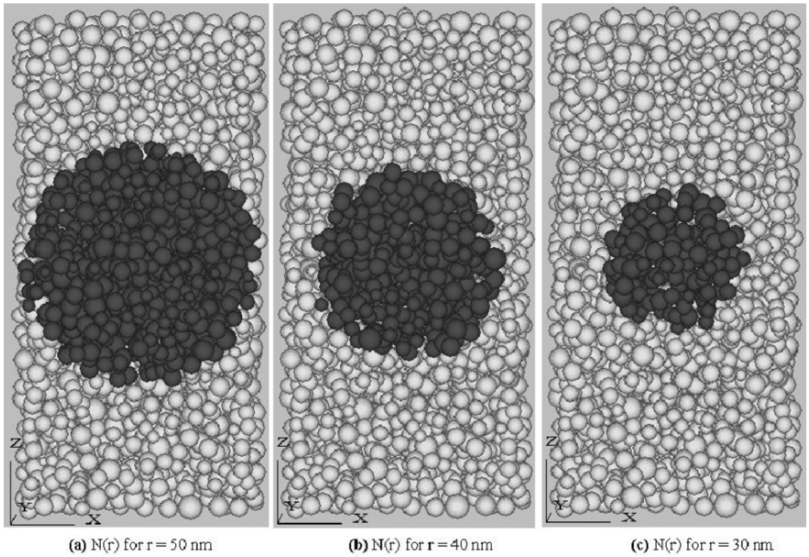

Fig. 10.24. Plan view for identifying secondary nanoparticles (*dark in color*) in aerogel cluster within varying radii of spherical regions

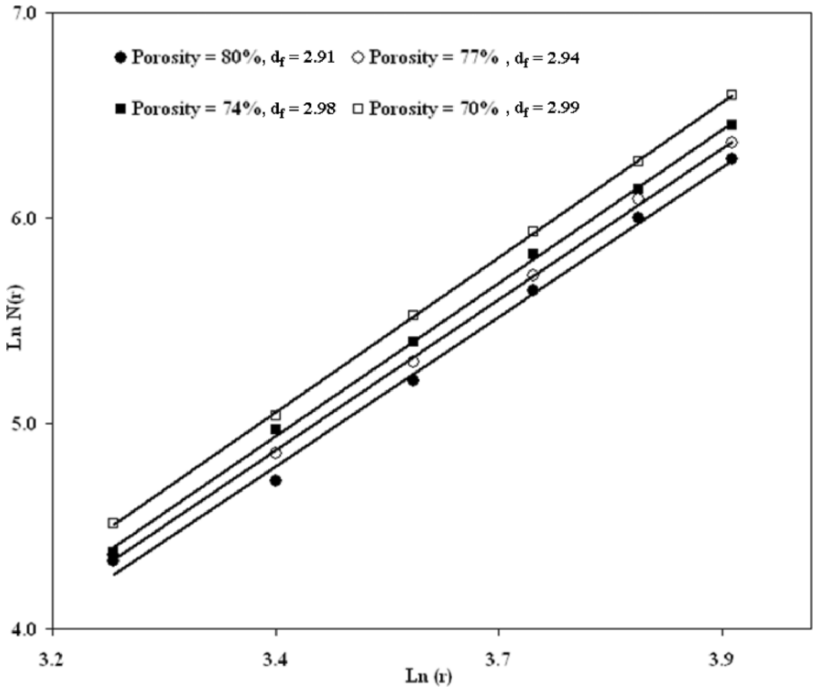

Fig. 10.25. Aerogel secondary particles distribution as a function of radial distance for clusters generated from DLCA with different initial cluster porosity

The fractal dimension (d_f) of the aerogel structure was found to decrease as the initial cluster porosity increases, as shown in Fig. 10.26. The figure confirms that aerogel structures become more fractal with increasing cluster porosity, as might be expected. This figure also reveals that the fractal dimension of an aerogel structure will asymptotically approach 3 with decreasing initial cluster porosity. As porosity represents the extent of void space, the aerogel cluster density decreases with increasing cluster porosity, which is intuitive. The trends observed in this study of fractal dimension of mesoporous aerogel structure are corroborated by similar observations for silica glass, reported in [5].

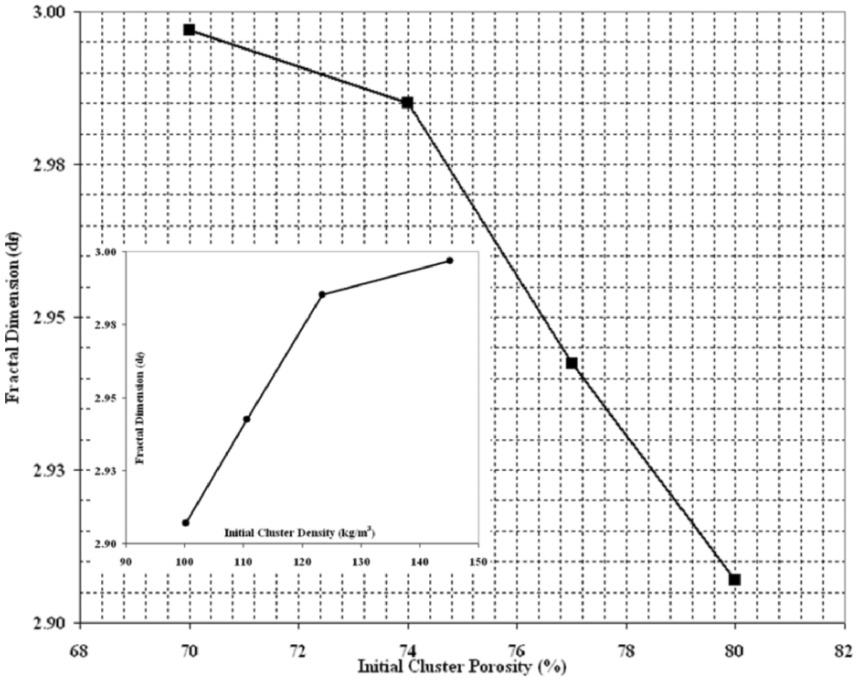

Fig. 10.26. Variation of fractal dimension of aerogel structure with initial cluster porosity (the *inset* shows the variation of fractal dimension with initial cluster density)

Finally, parametric sensitivity analyses were performed with changing x-aerogel cluster porosity. As shown in Fig. 10.27, numerical simulation of x-aerogel with 80% initial cluster porosity agrees well with the experimental response up to a strain level of 35%. At higher strain level, numerical results with 70% initial cluster porosity closely match with the experimental curve. During the compression experiment, the cluster porosity should decrease gradually, as depicted earlier in Fig. 10.5. The numerical model was unable to exactly replicate this porosity variation. Therefore, a slight mismatch between the experimental and numerical model, as shown in Fig. 10.27, is not surprising. The numerical model was found to offer a softer response with increasing cluster porosity, as might be expected.

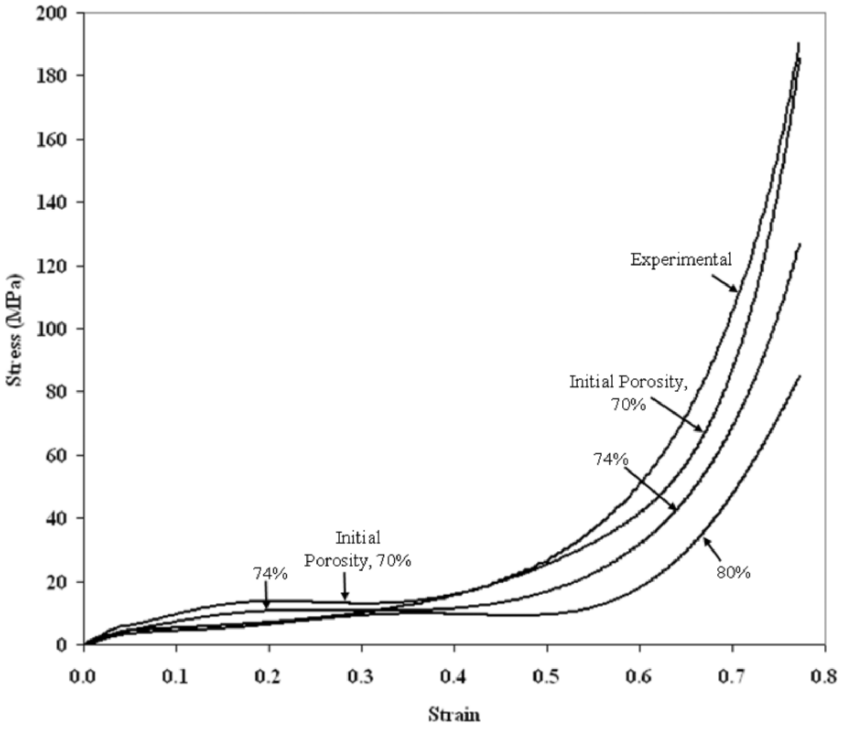

Fig. 10.27. Sensitivity analyses with changing initial cluster porosity

A summary of the parametric sensitivity analyses, discussed above, is presented in concise form in Table 10.5 below.

Table 10.5. Parametric sensitivity analyses through numerical simulation of aerogel

Variable parameter	Variation range (% change)	Variation of max. stress at 77% strain level (% change)
Particle contact stiffness, equal increment both in normal (k_n) and shear (k_s) directions	50–200 N m^{-1} (300%)	55–195 MPa (255%)
Ratio of normal stiffness to shear stiffness (k_n/k_s), where normal stiffness (k_n) was kept constant at 150 N m^{-1}	1–6 (500%)	No significant change
Ratio of shear stiffness to normal stiffness (k_s/k_n), where shear stiffness (k_s) was kept constant at 150 N m^{-1}	1–6 (500%)	190–90 MPa (–53%)
Bond strength	300×10^8 to 300×10^{12} MPa	Significantly reduced bond breakage
Friction coefficient	0.1–1.0 (900%)	130–270 MPa (108%)
Particle mass density	100–480 kg m^{-3} (380%)	No significant change
Cluster porosity	70–80% (14.3%)	185–85 MPa (–55%)

Only one parameter was changed at a time, while other parameters were held constant (see Table 10.4).

10.7 Conclusions

Aerogel is reported as one of the lightweight materials which can be used for different engineering applications. This chapter briefly describes the improvement of mechanical properties of silica aerogel by crosslinking its nanosize secondary particles with polymeric tethers. However, the stiff-

ness and strength of x-aerogel material strongly depend on its microstructural features, such as mesoporous cluster assemblies and particle connectivity, which can be evaluated by determining the fractal dimension. Each particle cluster generated from DLCA signified distinct network connectivity in terms of fractal dimension. A mesoporous aerogel structure was found to become more fractal with increasing initial cluster porosity.

Uniaxial compression experiment was conducted on x-aerogels to collect the basic mechanical properties. During the compression test, x-aerogels were found to behave as linearly elastic under very small strains (<4%) and then exhibited yielding followed by densification and inelastic hardening. The compressive strength of x-aerogels was found to be greatly improved to 186 MPa compared with native silica aerogels of 4 MPa, with only a 2.5 times density increment. The specific compressive strength of x-aerogels was also found to be higher than most other conventional materials. Effects of strain rate and temperature on the compression experimental response were also studied. The mechanical behavior of x-aerogels was unaffected within the strain rate range investigated.

In this study, numerical simulations were performed using particle mechanics to develop the structure–property relationship of nanostructured x-aerogel. First, a cluster of nanoparticles was generated in DLCA and then imported into PFC^{3D} for simulating the compression experiment. Good agreement was observed between the experimental and numerical results in terms of stress and strain data. The numerical model was then used to conduct a series of parametric sensitivity analyses by varying different parameters, including particle contact stiffness, bond strength, friction coefficient, particle mass density, cluster density, and cluster porosity. The particle contact stiffness was found to be an important factor affecting the failure mechanism. The numerical model offered stiffer response as the particle contact stiffness increased, predominantly in the normal direction. Reduced bond breakage was observed during the compression as the bond strength increased. The numerical model offered stiffer response with increasing particle frictional coefficient. The secondary particle density itself was found ineffective in the compression response. As porosity represents the amount of void space, the numerical model of the aerogel particle clusters predicted a softer response with increasing initial cluster porosity, and, consequently, with decreasing aerogel fractal dimension.

Acknowledgments

This study was funded by a research contract from NASA-Glenn Research Center. The contributions of Mr. Nilesh Shimpi, Mr. Atul Katti, Dr. Nicholas Leventis, and Dr. Hongbing Lu are hereby acknowledged.

References

1. Bouaziz J, Bout-ret D, Sivade A, Grill C (1992) Doping of partially densified aerogels: impregnation by solutions or by xerogel. Journal of Non-Crystalline Solids 145, 71–74
2. Ferry JD (1980) Viscoelastic Properties of Polymers, 3rd edition, Wiley: New York
3. Itasca (2003) Particle flow code in 3 dimensions. Version 3.0, User's Manual, Itasca Consulting Group
4. Katti A, Shimpi N, Roy S, Lu H, Fabrizio EF, Dass A, Capadona LA, Leventis N (2006) Chemical, physical, and mechanical characterization of isocyanate crosslinked amine-modified silica aerogels. Chemistry of Materials 18, 285–296
5. Kieffer J, Angell CA (1998) Generation of fractal structures by negative pressure rupturing of SiO_2 glass. Journal of Non-Crystalline Solids 106, 336–342
6. Leventis N, Sotiriou-Leventis C, Zhang C, Rawashdeh A (2002) Nanoengineering strong silica aerogels. Nano Letters 2, 957–960
7. Meakin P, Family F (1987) Structure and dynamics of reaction-limited aggregation. Physical Review A 36, 5498–5501
8. Roy S, Shimpi N, Katti A, Lu H, Rahman M (2006) Mechanical characterization and modeling of isocyanate-crosslinked nanostructured silica aerogels. In: 47th AIAA/ASME/ASCE/AHS/ASC Structures, Structural Dynamics, and Materials Conference, 14th AIAA/ASME/AHS Adaptive Structures Conference, 7th AIAA Gossamer Spacecraft Forum, 2nd AIAA Multidisciplinary Design Optimization Specialist Conference, 8th AIAA Non-Deterministic Approaches Conference, Newport, RI
9. Ruben GC, Hrubesh LW, Tillotson TM (1995) High resolution transmission electron microscopy nanostructure of condensed-silica aerogels. Journal of Non-Crystalline Solids 186, 209–218